Renewable Energy xxx (xxxx) xxx

Contents lists available at ScienceDirect

Renewable Energy

journal homepage: www.elsevier.com/locate/renene

A detailed study of tidal turbine power production and dynamic loading under grid generated turbulence and turbine wake operation

Matthew Allmark [a, *], Robert Ellis [a], Tim Ebdon [a], Catherine Lloyd [a], Stephanie Ordonez-Sanchez [b], Rodrigo Martinez [b], Allan Mason-Jones [a], Cameron Johnstone [b], Tim O'Doherty [a]

[a] Cardiff School of Engineering,Cardiff University, The Parade, Cardiff, Cf24 3AA, UK
[b] Department of Mechanical and Aerospace Engineering, University of Strathclyde, 75 Montrose St, Glasgow, G1 1XJ, UK

ARTICLE INFO

Article history:
Received 13 July 2020
Received in revised form
11 November 2020
Accepted 11 December 2020
Available online xxx

Keywords:
Horizontal axis tidal turbine
Lab-scale testing
Turbulence
Tidal turbine wakes
Control

ABSTRACT

The paper presents an experimental campaign developed to contribute to the current research considering the operation of Horizontal Axis Tidal Turbines within stochastic flow conditions, namely turbulent and wake induced flows. The campaign was conducted at approximately a $1/20^{th}$-scale within a recirculating flume. Experiments were conducted over five differing setups, yielding a baseline low Turbulence Intensity case, two high turbulence cases and two upstream device generated wake cases. The experiments were conducted at a range of differing rotor velocities established, in a novel way, by utilising both fixed speed and fixed braking torque control. The paper presents analysis of flow measurements to statistically quantify the stochastic flow conditions impinging on the model-scale tidal turbine. The power, thrust, torque and blade root bending moment of single blade were recorded and analysed against the flow conditions generated under the five cases. The analysis showed that it may well be possible to exploit the accelerated region around an upstream turbine to capture marginally higher power (6% increase) from downstream turbines. Lastly, it was found that the control scheme adopted has a significant impact on power and load fluctuations observed at differing rotor velocities.

1. Introduction

Energy extraction from the ocean's tides has gained widespread acceptance as a potential contributor to the UK energy mix [9]. The EU Renewable Energy Directive has recently extended previous commitments to stipulate that the EU community will fulfil 35% of its energy needs via renewable sources by 2030; it is foreseen that tidal energy extraction could go some way to helping achieve this target [10].

In order to achieve the 20 year lifespan [14] - quoted as being required for cost effective energy extraction - whilst reducing device over-engineering, detailed understanding of HATT operational loads is required. Contribution to the understanding of turbine performance and loading under realistic flow conditions, particularly with respect to turbulence and wakes, is the major focus of the presented research.Turbulent and wake flow conditions have been studied to within research via lab-scale testing, numerical modelling and large scale device data analysis. Indeed this area of research has been studied thoroughly through over the last 15 years [3,4,7,11–13,17,19–23].

The previous research elucidates the dynamic interaction and influence TI and length scales have on turbine operation. To characterize the performance of the CEMERG turbines, as discussed in this paper, the aforementioned research will be complemented by further experimentation. To further investigate the influence of turbulence on HATT operation this research supplements the current research by considering the impact of utilising differing control methodologies when operating in turbulent flows.

The paper proceeds as follows, the next section, Section 2 presents an overview of the experimental methodology and setup. The methodology section is followed by a two part discussion of the obtained experimental results, the initial results section, Section 3 presents analysis and discussion of the fluid velocity measurements gathered for each case. This is followed by the second results

* Corresponding author.
E-mail addresses: allmarkmj1@cf.ac.uk, matthew.j.allmark@gmail.com (M. Allmark).

https://doi.org/10.1016/j.renene.2020.12.052

Nomenclature

λ	Tip-Speed Ratio
T	Total Time, s
$\mathscr{K}$	Wave Number, m
$\mathscr{L}_x$	Integral Length Scale, m
$\mathscr{T}$	Integral Time Scale, s
$\overline{U_x}$	Mean fluid velocity, ms^{-1}
ρ	Fluid density, kg m^{-3}
τ	Rotor Torque, N
c	Chord Length, m
C_p	Non-Dimensional Power Coefficient
C_T	Non-Dimensional Thrust Coefficient
C_θ	Non-Dimensional Torque Coefficient
$C_{M_{Y\ Bi}}$	Non-Dimensional Bending Moment Coefficient blade i
C_{XY}	Cross-Correlation of X & Y
D	Rotor Diameter, m
f	Frequency, Hz
G	Power Spectral Density
$M_{Y\ Bi}$	Out-of-plane blade root bending moment blade i, Nm
N	Total Number of Samples
n	Sample number
R	Correlation Coefficient
r	Rotor Radius, m
T	Thrust, N
t	Time, s
t'	Time lag, s
TI	Turbulence Intensity%
U_x	Instantaneous fluid velocity, m s^{-1}
u_x'	Fluid Velocity Fluctuating Component, ms^{-1}

section, Section 4, which presents detail analysis of the lab-scale HATT performance and loading under the various test cases with Sections 4.1 and 4.2 present time domain statistics whereas Sections 4.3 and 4.4 detailed frequency domain analysis of the results. Lastly, the conclusions draw from the experimental campaign are presented in Section 5.

2. Methodology

2.1. Experimental setup

To understand the effects of grid generated turbulence and combined turbulent and wake flow regimes on HATT operation, a series of lab-scale experiments were undertaken at the IFREMER flume tank, Boulgne-Sur-Mer. A schematic of the IFREMER flume tank is presented in Fig. 1a. The flume has a working section of $2m \times 4m \times 18m$ and uses two pumps to generate flow velocities between 0.1 to $2.2ms^{-1}$. Flow straighteners are adopted to achieve regulated TI of approximately 1.5% [20].

The scale model HATT was mounted in the flume, as shown in Fig. 1b, via a 0.105 m diameter stanchion at a hub depth of 1 m. A Laser Doppler Velocimeter (LDV) was used to measure the fluid velocity prior to and during the experiments. The plan view schematics illustrated in Fig. 2 show the 5 experimental setups utilised to achieve a range of turbulence and wake in-flow conditions. For all cases the inlet fluid velocity was set to 1.1 m/s.

Five test cases were developed and tested as part of the research presented. Initially, Case 1 was undertaken - here, only the flow straighteners were installed leading to a low TI case. Case 1 is therefore the baseline case. Cases 2 and 3 were achieved via the

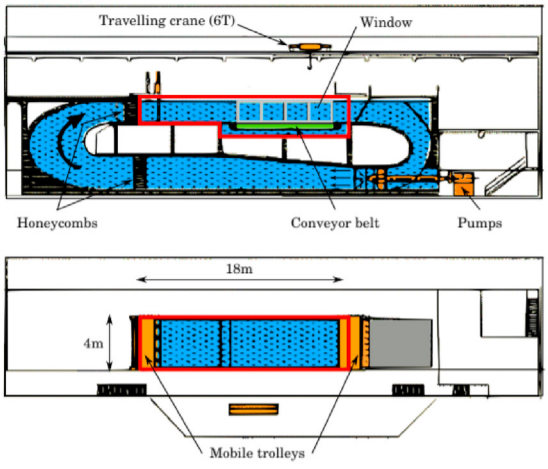

(a) Schematic of the flume at the IFREMER test facility, Boulogne-Sur-Mer.

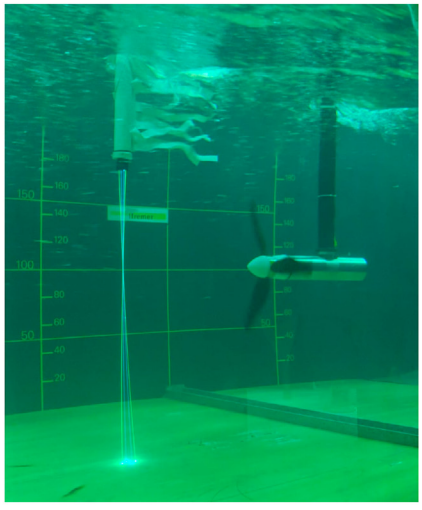

(b) An illustrative photograph of the experimental setup adopted at the IFREMER flume in Boulogne-Sur-Mer.

Fig. 1. Figures providing an overview of the Experimental Setup.

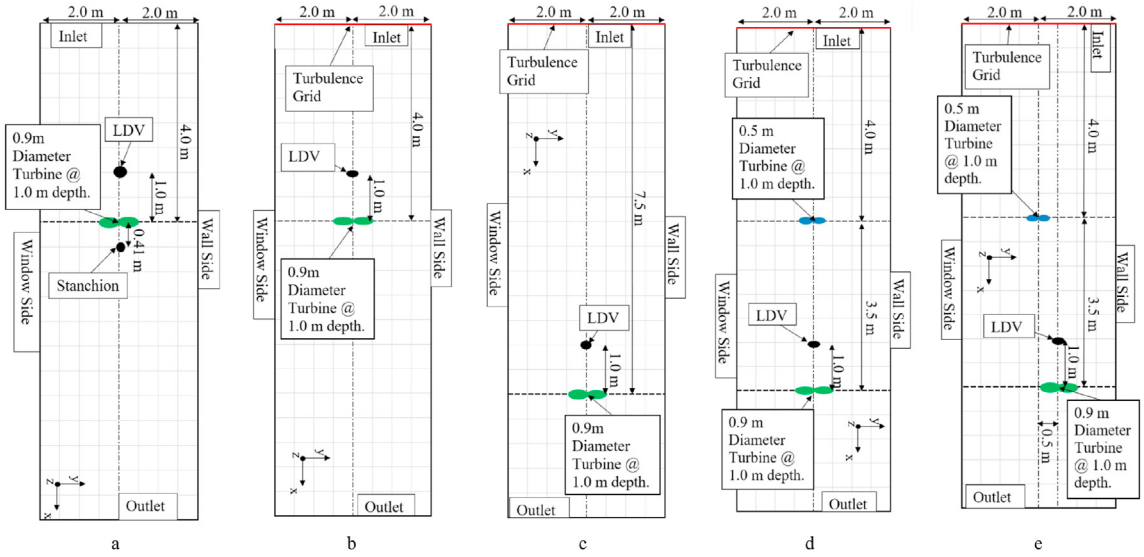

Fig. 2. A series of plan view schematics of the setups for the various test cases undertaken. (a) Case 1, (b) Case 2 (c) Case 3, (d) Case 4 and (e) Case 5.

installation of a turbulence generation grid. The details of the grid are presented in A and were based on the study undertaken in Ref. [4]. As can be seen in Fig. 2b and c, different inflow turbulence characteristics were developed by testing the HATT at two distances downstream of the turbulence grid, 4 m and 7.5 m for Cases 2 and 3, respectively. A further two test cases were created combining turbulence grid and HATT wake inflow conditions.

A second turbine, of 0.5 m diameter, was installed 4 m downstream of the turbulence grid to generate a wake. For brevity, as no measurements are presented from the 0.5 m HATT details of the turbine are omitted, however a full set of details of the 0.5 m diameter turbine can be found in Ref. [2]. The 0.9 m diameter turbine was positioned 3.5 m (7 diameter) downstream of the 0.5 m diameter turbine. For Case 4 the downstream turbine was installed directly behind the 0.5 m diameter turbine and in Case 5 the downstream turbine was offset in the cross stream direction by 0.5 m as seen in Fig. 2. The differing diameters of upstream and downstream devices were utilised as these were the devices available at the time of testing, moreover the flow data captured in the wake of the smaller device was used to validate the computational fluid dynamics analysis detailed in Ref. [8] and therefore had to maintain geometric similarity.

Measurements of the turbine performance were taken at a range of operating conditions achieved utilising speed control (**SC**) and torque control (**SC**) of the HATT. The device control was achieved by the incorporated Permanent Magnet Synchronous Machine (PMSM) housed in the device nacelle and directly coupled to the rotor.control refers to device control where the goal of the system is to maintain a constant set-point rotational velocity. This was achieved via velocity feedback control loop with a proportional integral controller, the time constant of which was set to 2.7 ms. Torque control refers to device control where the braking torque developed by the PMSM was maintained at a constant value - therefore the device rotational velocity was allowed to change. This control type was achieved via vector oriented control as detailed in Ref. [18] with a loop execution rate of 500 μs. Within Table 1 the speed control cases are detailed in terms of rotational velocity. The torque control cases are detailed in terms of the torque value set by the PMSM for the given test. Turbine data and LDV data as detailed in the preceding sections were captured for each of the aforementioned operational settings for 200 s.

Table 1
A table detailing the operating points for which data was captured for each test set up case.

	Speed Ctrl Cases, $rads^{-1}$	Torque Ctrl Cases, Nm
Case 1	0.0, 2.4, 3.6, 4.9*, 6.1, 7.3 9.8*, 12.2, 14.6, 17.1*, 21.9^{FW}	10.0, 12.5, 15.0, 17.5, 20.0
Case 2	0.0, 5.7*, 6.8, 7.9, 9.1*, 10.2, 11.3*	10.0, 12.5*, 15.0*, 17.5*, 18.0
Case 3	0.0, 5.7*, 6.8*, 7.9*, 9.1, 10.2, 11.3	10.0, 12.5*, 15.0*, 17.5*, 20.0
Case 4	0.0, 5.7*, 6.8*, 7.9*, 9.1*, 10.2*, 11.3*	10.0, 12.5*, 14.0*, 15.0*
Case 5	0.0, 5.7*, 6.8., 7.9, 9.1*, 10.2, 11.3*	10.0, 12.5*, 15.0*, 17.5*, 20.0

*repeated test case to verify repeatability. FW - Freewheeling.

2.2. Instrumented lab-scale HATT

The lab-scale HATT, which was the focus of this study, utilised a three bladed rotor of 0.9 m diameter. The blades are of length 385 mm with a hub diameter of 130 mm. The blade profile is based on a Wortmann FX63-137, the chord length, twist distributions and the design process detailed in Ref. [1]. The turbine rotor plane was situated 434 mm from the stanchion centre.Operation of the HATT was controlled via a PMSM integrated into the nacelle. Within the nacelle the rotor was directly coupled to the PMSM creating a direct drive device. The PMSM was used to extract energy from the turbine rotor and operated in either speed or torque control. Control of the PMSM was achieved via servo control and back-to-back voltage source converters. A control loop performing Vector Oriented Control (VOC) was used to control the braking torsion applied and energy extracted by the PMSM. An additional speed control loop could also be included to vary the braking torque applied by the PMSM to maintain a set point rotational velocity. The tests were undertaken at a variety of average rotational speeds, achieved via both speed control and torque control of the PMSM, detailed formulations of the control strategies of the turbine can be found in Ref. [18]. Table 2 details the turbine parameter as well as the instrumentation recorded during the experimental campaign

Table 2
Table outlining the main design specifications and Instrumentation List for the developed HATT.

Specification	Details
Rated Flow Velocity	Continuous: 1.3 ms^{-1} Instantaneous: 1.5 ms^{-1}
Rated Power	0.6 kW
Maximum Rotational Velocity	350 RPM
Rated Torque	Continuous: 41 Nm Instantaneous: 54 Nm
Maximum Rotor Thrust	1.07 kN
Maximum Blade Root	Flapwise: 129.76 Nm
Bending Moment	Edgewise: 18.13 Nm
Sample Rate	200 Hz
Load Measurements	
Control Types	Speed Control, Torque Control Regulated Torque Control Optimal λ control
Instrumentation List	
Instrumentation Data:	
Blade root bending moment, Blade 2 (M_{YB2});	
Rotor Thrust; Rotor Torque; Rotor Position; Rotational Velocity	

presented. Full details of the 1/20th scale HATT instrumentation along with calibration and uncertainty details can be found in Ref. [1].

2.3. Fluid velocity measurements

During each of the test cases the fluid velocity within the flume was measured via a two axis LDV. The LDV system used was a 2D DANTEC FiberFLOW, provided by IFREMER, and calibrated by the manufacturer to $\pm 0.001 ms^{-1}$. The measurement control volume created via the coincidence of the LDV lasers was 500 mm from the head of the device. The control volume through which a particle must pass in order for a measurement to be made was $0.12mm \times 0.12mm \times 2.51mm = 0.04mm^3$. The device does not have a fixed data rate; however sufficient seeding of the flume afforded mean and median sample rates of 160 Hz and 350 Hz in the stream-wise direction, respectively. The re-circulating flume was seeded with silver coated glass spheres of 10 μm in diameter. The LDV was setup to measure the stream-wise and cross-stream fluid velocity components. The probe was submerged to a depth of 0.5 m and mounted 1 m upstream of the turbine during the experiments - this resulted in gathering flow measurements 1 m upstream of the turbine in-line with the centre of the 0.9 m diameter rotor.

To supplement the fluid velocity measurements taken during the test cases a series of fluid velocity characterisation measurements were undertaken prior to turbine installation for each of the 5 cases detailed in Fig. 2. The inflow for the baseline case, Case 1, was characterised by taking a point LDV measurement at the centre of eventual turbine rotor plane. The measurement was taken 4 m downstream of the turbulence grid with the measurement volume centred at 1 m depth and 2 m across the flume. The on-coming fluid velocity in Cases 2 and 3 were characterised via LDV measurements taken along the centre line of the flume. The measurements were taken with measurement volume of the LDV set to hub depth (1 m depth) at differing distances downstream of the turbulence generation grid. To characterize the wake flow prior to downstream turbine installation a series of measurements were taken at intervals across the flume again with the LDV measurement volume set at the turbine hub depth and at 7 diameter downstream of turbine 1. The results of these measurement are presented in Section 3.

Table 3
A table detailing the flow characteristics observed during pre-turbine installation LDV measurements.

Unit	$\overline{U_x}$	RMS_x	$\overline{U_y}$	RMS_y	TI_x	$\mathscr{L}_x$	Record length
	ms^{-1}	ms^{-1}	ms^{-1}	ms^{-1}	%	m	s
Case 1	1.11	0.02	−0.03	0.01	1.5	0.48	120
Case 2	1.02	0.12	−0.02	0.11	11.7	0.20	1000
Case 3	1.07	0.08	−0.01	0.07	7.10	0.19	1000
Case 4	0.85	0.12	0.01	0.12	13.24	0.16	400
Case 4*	0.99	0.12	0.00	0.10	11.95	0.24	
Case 5	1.11	0.10	−0.03	0.08	9.03	0.31	99
Case 5*	1.15	0.09	−0.01	0.08	9.78	0.22	

*Volumetrically Average Quantities.

3. Flow measurement analysis

3.1. Stream-wise mean velocity and TI

The mean stream-wise fluid velocity and TI for a time series, $U_x(n)$ of length N samples are defined in Equations (1) and (2).

$$\overline{U_x} = \frac{1}{N}\sum_{n=1}^{N} U_x(n) \tag{1}$$

The measured fluid velocity time series can be decomposed into a mean quantity and a fluctuating quantity as follows, $U_x(n) = \overline{U_x} + u_x'$. Where, $\overline{U_x}$ is the mean velocity in the stream-wise direction and u_x' is the instantaneous deviation from the mean flow velocity value in the stream-wise direction. By definition, $\overline{u_x'} = 0$. The associated stream-wise TI can be defined as in Equation (2):

$$TI = \frac{\sqrt{\overline{u_x'(n)^2}}}{\overline{U_x}} \tag{2}$$

The mean stream-wise fluid velocities and turbulence intensities were calculated for each of the test cases, the results of the calculations can be found in Tables 3 and 4. Fig. 3 shows the mean stream-wise fluid velocities (blue) and TIs (red) calculated using the prior flow survey data (lines) and via the LDV data captured during the turbine experiments (points). The data points at 3 m and 6.5 m downstream of the turbulence grid correspond to Cases 2 and 3, respectively. The results show that the presence of the turbine had a large impact on the mean fluid velocity recorded during turbine testing. Clearly the flow reduces immediately upstream of the turbine as expected with the presence of an object in a flow. The effect of the turbine presence had a minimal impact on the measured TI values when compared to the flow measurements taken prior to turbine installation. Due to these findings, for Cases 2 and 3, the prior survey results are utilised in Section 4.1 when calculating non-dimensional performance coefficients.

Fig. 4 shows the mean fluid velocity recorded in the wake of the upstream turbine installed to achieve Cases 4 and 5. The figure shows the results of a transect measured prior to turbine installation. Also plotted are the mean flow velocities measured during the Case 4 and 5 experiments and the results of volumetric averaging of the wake transect data. The procedure followed in calculating the volumetric averages can be found in Ref. [16]. Again, due to the effect of the turbine and the velocity gradient along the wake, the measurements taken during the experiments show a large deficit when compared to the prior wake survey measurements.

Table 4
A table detailing the flow characteristics observed upstream of the turbine during the experiments.

Unit	Control Type	$\overline{U_x}$	TI_x	$\mathscr{L}_x$	Record length
		ms^{-1}	%	m	s
Case 1	Speed Ctrl	1.06	2.0	0.80	130
	Torque Ctrl	1.12	1.6	0.70	130
Case 2	Speed Ctrl	0.94	15.8	0.16	200
	Torque Ctrl	0.93	16.0	0.15	200
Case 3	Speed Ctrl	1.02	8.0	0.24	200
	Torque Ctrl	1.01	7.9	0.21	200
Case 4	Speed Ctrl	0.65	19.0	0.14	200
	Torque Ctrl	0.65	19.0	0.15	200
Case 5	Speed Ctrl	1.07	9.5	0.23	200
	Torque Ctrl	1.06	9.6	0.22	200

Fig. 3. Average Stream-wise Flow velocity and TI measured downstream of the Grid. The lines show the centre line survey results recorded prior to turbine installation whereas the points show the measure quantities as measured 1D upstream of the installed turbine.

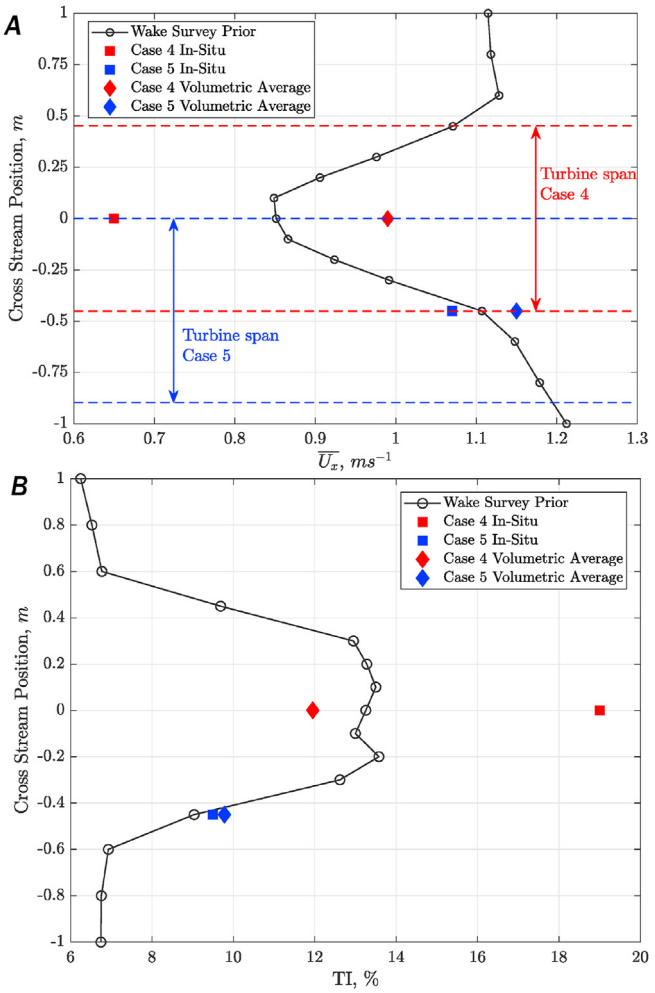

Fig. 4. Plots of (**A**) the mean stream-wise velocity, $\overline{U_x}$, and (**B**) stream-wise TI for the various fluid velocity measurements in the wake of the installed turbines for Cases 4 and 5.

Furthermore, volumetric averaging of the fluid flow gives a larger mean flow velocity compared to the given centre point mean velocity for each case. As discussed by various researchers [4,19], the volumetrically averaged flow velocities are likely to be a better indicator of the inflow conditions experienced by the turbine. As such, in Section 4.1 the volumetrically averaged fluid velocity estimates were used to calculate the non-dimensional performance parameter. Fig. 4 shows the turbulence intensities observed using the same data sources discussed. Case 4 shows significant deviation between the TI recorded during the turbine experiments and those recorded during the prior wake transects. The difference of 31 % suggests significant turbulent dissipation between the 1 m upstream measurement position and the measurements taken at the rotor position prior to installation. This is likely as the effect of the turbine on the values of TI measured in Cases 2 and 3 was insignificant. Case 5 shows some discrepancy between the prior transect and in-situ TI values observed, approximately 5 %, suggesting slower turbulence dissipation outside of the wake relative to the wake centre.

3.2. Integral length scale

The nature of turbulent flows can be further understood in terms of a local length scale, again this is a property of the flow and is related to the channel or blockage geometry associated with said flow. This length scale, known commonly as the Integral Length Scale, is a measure of the largest turbulent structures within flow, which decompose into smaller turbulent structures via non-linear dissipation [5]. In terms of HATTs, it is has been reported that the largest turbulent structures, as characterised by the integral length scale, are significant in generating changes in turbine performance and could possibly be the dominant driver of dynamic loading [4]. An estimate of the integral length scale can be developed from the consideration of a measured fluid velocity time series at a single point. In such a manner the integral time-scale, in seconds, can be defined in terms of the auto correlation of a given flow velocity time-series, as in Equation (3) [29].

$$\mathscr{T} = \int_0^{\mathbf{T}} R(t') \cdot dt' \tag{3}$$

$$R(t') = \frac{\overline{U_x(t)U_x(t-t')}}{\overline{U_x^2}} \tag{4}$$

The integral time scale can be multiplied by the time-averaged fluid velocity to yield a length scale in metre, $\mathscr{L}_x = \mathscr{T} \cdot \overline{U_x}$.

The calculation of the integral time scale, as defined in Equation

(3), requires the integral to converge to a finite value. To ensure this any correlations related to experimental noise should be emitted from the integral. This can be done as outlined in Ref. [4], where the upper limit of the integral, **T**, is defined as the lag value observed, $t_{R_{Thresh}}$, where the correlation function, $R(t')$, falls below a defined threshold, R_{Thresh}. The value of R_{thresh} was set by observing the mean correlation coefficient between two fluid velocity time-series, measured using the LDV setup discussed in Section 2.1. The two time-series used were related to Case 1, with no Grid, and Case 2, 4 m downstream of the turbulence grid, which should be uncorrelated other than any inherent correlation between captured signals from the same measurement system. The results of this process yielded a suitable threshold of $R_{Thresh} = 0.04$. An estimate of the integral length scale in metres was developed for each of the cases tested. The results of the calculations are summarised for each case within Tables 3 and 4

3.3. Wave number spectra

The power spectral density (PSD) of a signal, in this case the fluid velocity measurements taken for each of the cases at a single point, can be defined as the Fourier transform of the auto-correlation function of a given signal, as defined in Equation (4). The PSD can be written as in Equation (5), in-terms of Wave number, $\mathscr{K}$. The wave number is defined, using Taylor's hypothesis, as $\mathscr{K} = \frac{f}{U_x}$. The application of Taylor's hypothesis to the experimental data captured, results in the assumption that the *TI* values observed in the experiments are small enough to assume that the spatial spectra of the turbulence can be approximated by the wave number spectra as calculated for a measurements taken at single point [28].

$$G(\mathscr{K}) = \int_{-\infty}^{\infty} R(t') \cdot e^{-i\mathscr{K}t} \cdot dt \tag{5}$$

The PSD is useful in understanding the distribution of turbulent energy over a range of frequencies or wave numbers. This facilitates an understanding of a large range of turbulent structures or eddies sizes, as characterised by their wave number, and their contribution to the overall turbulent energy within the flow.

In general the wave number spectra observed for each case follow the $-5/3$ gradient for $\mathscr{K} > 10$ as predicted by Kolmogorov [15]. This suggests that in general the inertial sub-range was captured with $-5/3$ gradient appearing regardless of the structure of the energy generating mechanism [5,15,28,29]. An anomaly in this regard were measurements taken during the pre-characterisation of Case 5, in Fig. 5**A** higher energy density was observed for $\mathscr{K} > 100$ causing the curve to deviate from the aforementioned $-5/3$ gradient. This is likely to have been a result of having a captured too short a time series - which is was due to timing constraints during the test campaign.

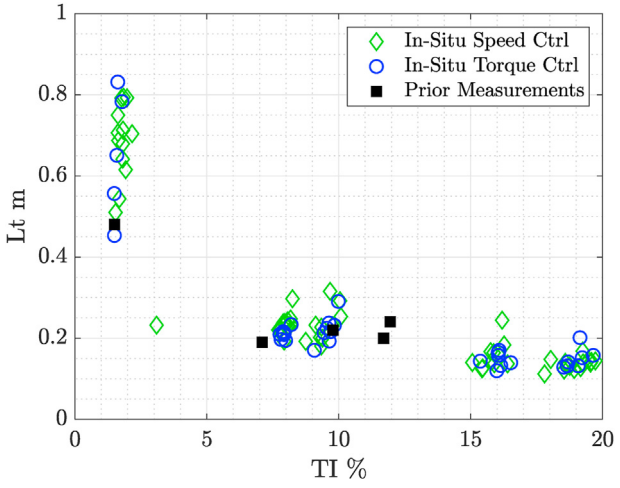

Fig. 6. Integral Length scale plotted against TI for each of the cases.

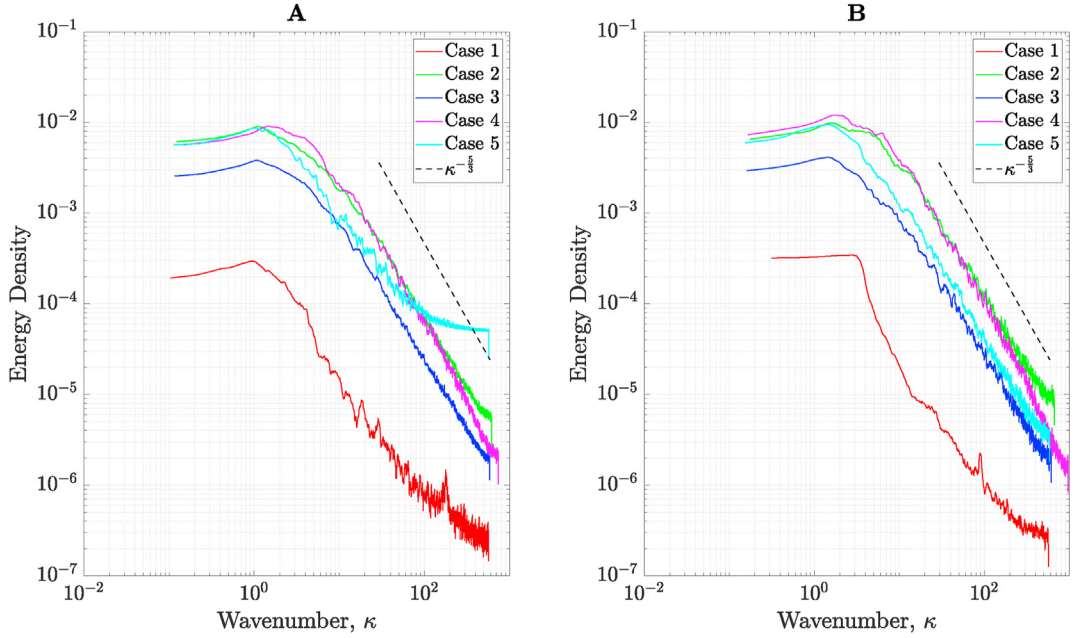

Fig. 5. Figure showing the PSDs calculated for each of the 5 test cases. **A** Shows the data captured prior to turbine installation. **B** shows the data captured with the turbine installed during the experiments.

3.4. Grid generated turbulence

Behind the turbulence grid wakes are formed which interact and generate turbulent flow. Some distance downstream of the grid the turbulence structures interact transferring energy in some complex way with the turbulence becoming homogeneous as a result. The shear flow resultant from the reduced flow velocity close to the grid is the only source of turbulent energy generation downstream of the grid and as such the turbulent energy in the flow tends to decay. It is generally found that the rate of energy transfer to smaller eddies decreases inline with the turbulent energy decay - this tends to increase the size of the turbulent structures with distance downstream of the grid [5].

Fig. 6 shows that the results gathered are in agreement with the qualitative description of grid generated turbulence given above. The negative correlation between TI and $\mathscr{L}_x$ suggests decreasing TI with distance downstream of the grid coupled with growth of $\mathscr{L}_x$. In this way the strategy in the test plan was to achieve two TIs and $\mathscr{L}_x$ combinations by positioning the turbine at the 4 m and 7.5 m distances downstream of the grid. However, the growth in $\mathscr{L}_x$ with downstream position was incredibly slow, yielding similar $\mathscr{L}_x$ values for both cases. As such, and exacerbated by the inverse correlation between TI and $\mathscr{L}_x$, the separate effects of each were not studied within this paper.

3.5. Flow measurement summary

Tables 3 and 4 show the fluid flow quantities observed prior to turbine installation and during the HATT experiments. Each of the quantities was measured, or calculated, as described in the preceding sections.

4. Turbine performance analysis

4.1. Non-dimensional values

The non-dimensional analogues for the power, torque, thrust and blade root bending moments are considered to compare the turbine performance under the different flow conditions observed under each of the five test cases. The non-dimensional operating parameters are presented against Tip-Speed Ratio as defined in Equation (6) and are defined below in Equations (7)–(10).

$$\lambda = \frac{\omega \cdot R}{\overline{U_x}} \tag{6}$$

$$C_P = \frac{\omega \cdot \tau_{Rotor}}{0.5\rho A \overline{U_x}^3} \tag{7}$$

$$C_\theta = \frac{\tau_{Rotor}}{0.5\rho A R \overline{U_x}^2} \tag{8}$$

$$C_T = \frac{T}{0.5\rho A \overline{U_x}^2} \tag{9}$$

$$C_{M_{YB2}} = \frac{M_{YB2}}{0.5\rho A R \overline{U_x}^2} \tag{10}$$

Figs. 7 and 8, show the non-dimensional parameter for the rotor and are plotted against tip-speed-ratio, λ. Fig. 7 shows the non-dimensional quantities for the HATT rotor for the grid only cases compared to the no grid case for speed and torque control, respectively. Fig. 8 shows the non-dimensional parameter for the wake cases compared with the no grid case, again utilising speed and torque control, respectively. In each figure the upper charts show the mean values of the non-dimensional parameter, whereas the lower charts show the recorded standard deviation of the non-dimensional parameter.

In Fig. 7 the $\overline{U_x}$ quantity in Equations (7)–(9), used to calculate the non-dimensional parameter, was taken from point measurements captured at the turbine hub centre location prior to turbine installation - as noted in Table 3. This was considered suitable as it was assumed that the flow conditions generated by the grid had become homogeneous at the 4.0 m and 7.5 m downstream locations. This assumption is clearly not valid for the wake cases tested and as such volumetrically averaged values for $\overline{U_x}$ were used to calculate the non-dimensional parameter for Cases 4 and 5, as highlighted in Table 3.

In Fig. 7 the non-dimensional curves for the grid cases, Cases 2 and 3, are in relatively poor agreement with the initial non-dimensional curve recorded for the no grid case, Case 1. This would suggest that the prior assumption of homogeneous conditions at the downstream distances was likely to have been erroneous, resulting in a discrepancy between the fluid velocity value used to calculate the non-dimensional values via Equations (7)–(9). This is supported by the larger error observed for the C_P curves relative to the C_θ and C_T curves, which have $\overline{U_x}^3$ and $\overline{U_x}^2$ dependencies, respectively. Similar findings were observed in Fig. 7 for the Torque control cases - again further supporting the above findings. Good agreement between the mean non-dimensional parameter observed can be seen comparing speed and torque control. This agreement confirms the finding that the mean operational parameter are unaffected by the differing control strategies, as described in Ref. [24–27]. This has previously been reported for differing wave conditions and has now been confirmed under turbulent operating conditions. Whilst the in-variance of non-dimensional parameter to the two control strategies can be demonstrated using the data captured for Cases 1, 2 and 3, the effect of TI on mean quantities is difficult to comment on given the large discrepancy between observed non-dimensional parameter.

Intuitively, the standard deviations observed for each of the non-dimensional parameter, in Fig. 7, were found to increase with recorded TI, as noted in Table 3 and in agreement with the findings of [3]. The extent of this dependency is difficult to ascertain due to the aforementioned discrepancy in the reference flow velocity used in calculating the non-dimensional parameter. An increase in the observed standard deviation with TI was also found to be true for the torque control case for C_p and C_T, Fig. 7. However, whilst the two grid cases yielded higher standard deviations in the C_θ value relative to the no grid case when utilising torque control, the discrepancies between the two grid cases was found to be negligible. Furthermore, the standard deviation of C_θ recorded in the torque control cases were generally found to be an order of magnitude smaller than those observed under speed control for the two grid cases, yielding levels of variation in C_θ comparable to Case 1 under speed control. Comparisons of the standard deviations recorded for C_T between the speed and torque control cases, show that at $\lambda = 4$ (peak power) the torque control case yielded a standard deviation approximately 64 % larger than the speed control case for Case 2.

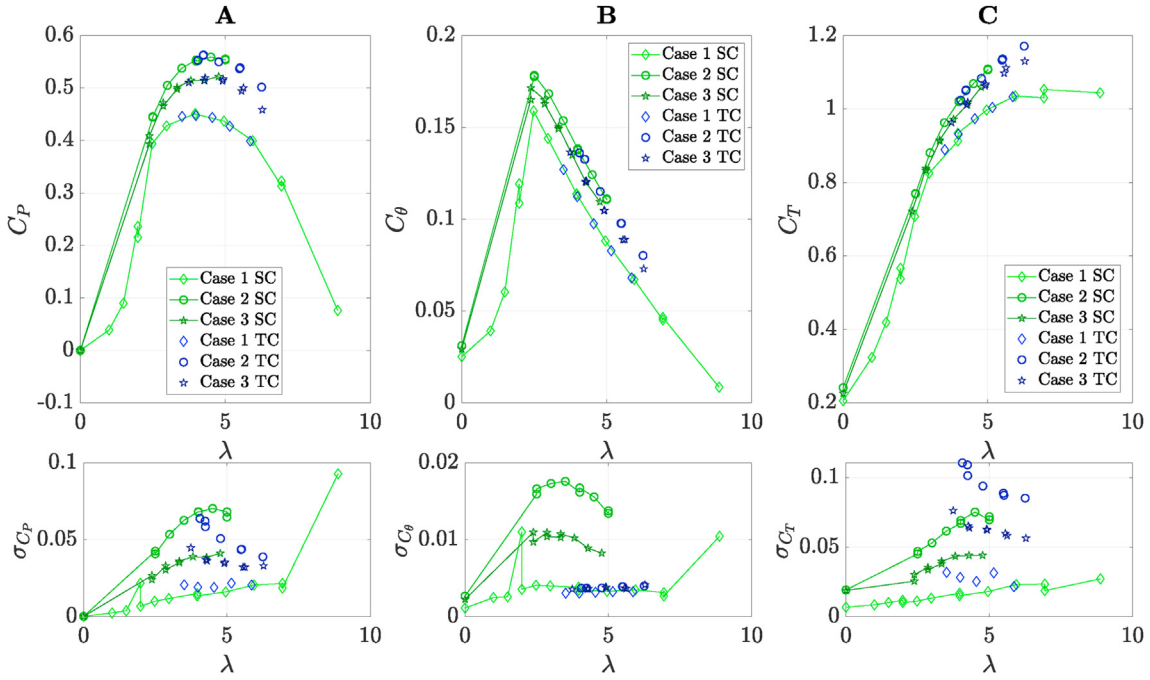

Fig. 7. Non-Dimensional curves observed, for test Cases 1, 2 and 3. The upper charts show mean values, the lower charts show standard deviations. (**A**)C_P vs λ (**B**)C_θ vs λ (**C**)C_T vs λ

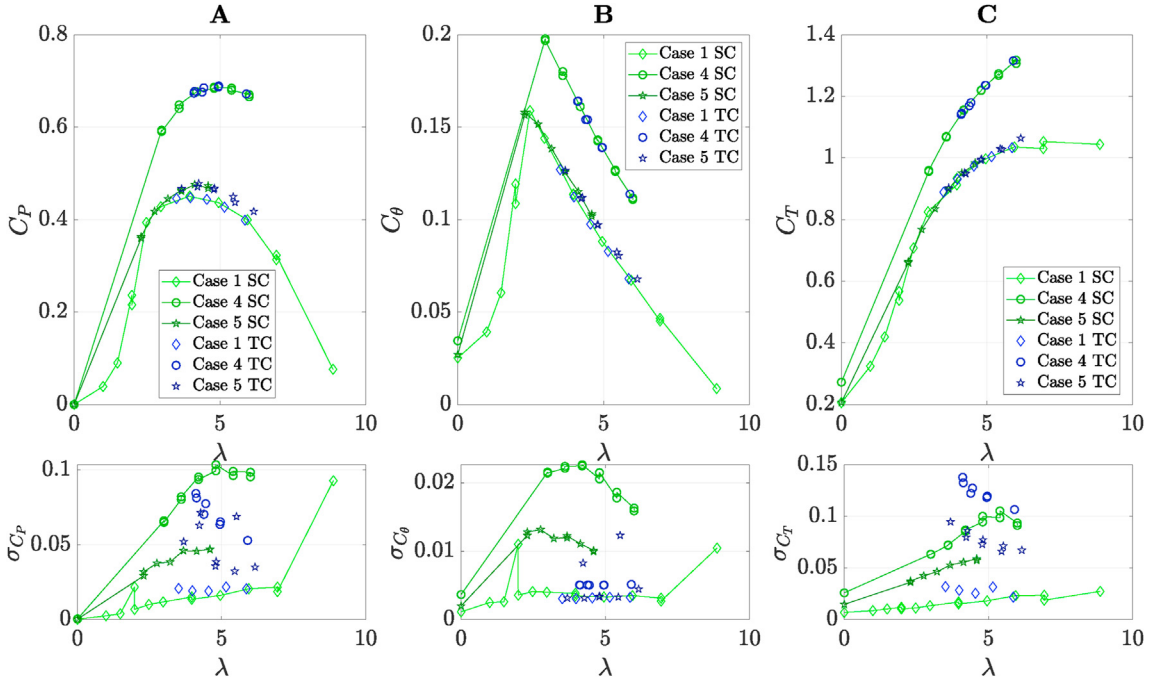

Fig. 8. Non-Dimensional curves observed, utilising speed control, for test Cases 1, 4 and 5. The upper charts show mean values, the lower charts show standard deviations. (**A**)C_P vs λ (**B**)C_θ vs λ (**C**)C_T vs λ

For the lower TI grid case, Case 3, this increase was approximately 75 % with the no grid case yielding an increase of 87 %. Similar levels of spread were found for C_P in both the speed and torque control cases around $\lambda = 4$ with the speed control case exhibiting a marginally larger spread for the higher TI case, Case 2. However, the torque control strategy yielded a slightly higher variation in C_P for both the low TI grid case and the no grid case - Cases 3 and 1, respectively.

The lowest λ values achievable prior to stall were found to increased with TI. λ values of 3.51, 3.74 and 4.06 were achieved for

Cases 1, 3 and 2, respectively. Generally, the spread of C_P and C_T was found to increase with decreasing λ setting under torque control. Under speed control a peak spread in the non-dimensional values can be observed - however, testing at higher λ values would be required to confirm this, with the position of the peak value varying for differing non-dimensional quantities.

In contrast to the grid only cases, Fig. 8 shows good agreement in non-dimensional performance coefficients for all three cases plotted, namely Cases 1, 4 and 5. This would suggest that the volumetric averaging approach utilised was sufficient in calculating appropriate normalising fluid velocities. Furthermore, the mean values of the non-dimensional parameter were found to be approximately equal under both speed and torque control, again highlighting the stability of mean non-dimensional parameter to the two control strategies utilised.

Similar characteristics were observed for the wake cases as the grid cases in terms of the standard deviations recorded for each of the non-dimensional parameter presented. The torque coefficient, C_θ, under the torque control experiments had a standard deviation, at $\lambda = 4$, an order of magnitude smaller than observed for the speed control operation for the two wake cases. Similar to the findings for Cases 1, 2 and 3, the levels of variation in C_θ when utilising torque control were of a similar size to those observed under speed control and no grid.

The spread in the thrust coefficient, C_T, at $\lambda = 4$ was found to be 25 % larger under torque control rather than speed control for Case 4. This difference was increased to 50 % for Case 5 and again was found to be approximately 86 % for Case 1. Power coefficient variations were larger for the full wake case, Case 4, when speed control was utilised. This finding did not extended to the partial wake case, Case 5, where similar levels of variation in C_P were observed for both control types.

Fig. 9 shows the non-dimensional coefficients, $C_{M_{YB2}}$ for the out of plane or flap-wise blade Root Bending Moment (RBM), against λ under speed control and torque control. Within the figure the left charts (**A**) relate to the grid Cases 2 and 3 compared to the no grid case, Case 1. The right plots (**B**) relate to Cases 4 and 5, again presented in comparison to the no grid case, Case 1.

Fig. 9 (**A**) shows a larger deviation of mean C_{M_x} for the grid cases relative to the no grid case than observed in Fig. 9(**B**) comparing the wake cases to the no grid case. The trend extending across Fig. 9 shows that this effect of utilising point based average fluid velocity or utilising a volumetrically averaged fluid velocity to normalise blade root bending moment is independent of the control strategy adopted. As expected the shape of the CM_{YB2} curves plotted follows that of the thrust coefficient plots in Figs. 7 and 8. Again, the standard deviations observed in the lower plots are generally proportional to the TI measured for the given case and λ value. An increase in the standard deviation of C_{M_x} was observed for the torque control cases relative to the speed control cases, this increase ranged from 15 % to 25 %. Interestingly, this increase in the spread of values is not proportional to the increase in the spread of C_T values observed when utilising torque control rather than speed control.

To further understand the nature of the variation in non-dimensional parameter for the grid and wake cases, under the differing control strategies, the standard deviation of λ - value against the mean operating λ was considered. It was immediately observed that, as expected, significantly larger oscillations in λ were recorded for the torque control cases relative to the speed control cases. The variation in λ under each control type was found to be proportional to the TI recorded for each case - however, the effect of TI had a much greater impact on λ variation under torque control. Under the torque control cases, the variation in λ was found to decrease with increased mean λ value, which is reminiscent of the structure observed for the variation in non-dimensional parameter for the same torque control case as presented in the lower plots within Figs. 7 and 8. Similarly, the trend in variation of the standard deviation of λ under speed control is similar to the trend in the standard deviation of the non-dimensional parameter presented in Figs. 7 and 8.

Significantly, analysis of the non-dimensional operating parameter for each of the cases for speed and torque control show that care should be taken in measurement and calculation of the normalising fluid velocity used in generating non-dimensional performance coefficients. This is particularly important when considering the mean flow velocity in grid generated and wake

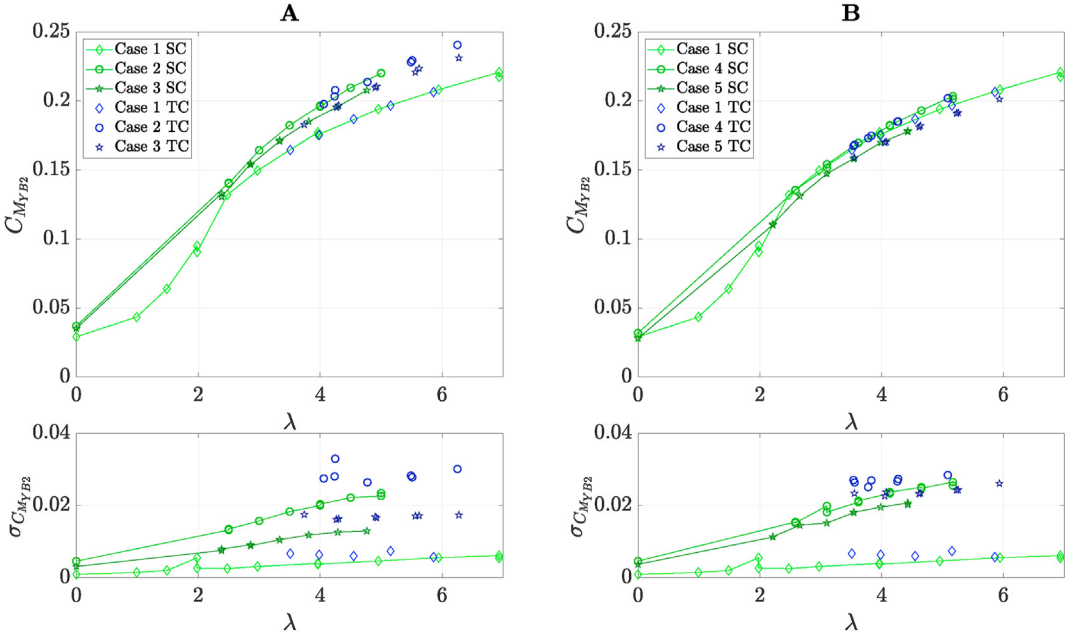

Fig. 9. Non-Dimensional blade root bending moment coefficients, utilising speed control. The upper charts show mean values, the lower charts show standard deviations. (**A**) Cases 1, 2 and 3 (**B**) Cases 1, 4 and 5.

generated turbulence cases. This is significant not only for flume testing but for large scale devices which are likely to operate in both temporally and spatially more stochastic flow regimes.

Furthermore, the analysis found some fundamental differences in the operation of the turbine under the differing control regimes. Whilst similar mean values were observed for the differing cases, the transient performance of the turbine, as quantified by the standard deviation of the non-dimensional parameters, varies significantly under the differing control cases. Particularly interesting is the negligible effect of control strategy on the spread of non-dimensional power coefficient, C_P around peak power for all cases, excluding Case 4, and both control types. This finding would suggest that the rotational speed variations in the torque control cases are similar in magnitude to the variation in torsion developed under the speed control cases, with the variation in rotational speed driving the variation in power produced under torque control and visa versa for speed control. It is also worthwhile noting the counter intuitive finding, that despite the turbine operating in the shear boundary of the wake of the 0.5 m diameter turbine in Case 5 (see Fig. 4 **A**), smaller variability in the non-dimensional parameter was found than under Case 4, whereby the turbine was operating predominantly in the wake.

The relative spread in thrust and torque coefficients in each of the control cases suggests that torsional oscillations arising from turbulent flows could be reduced by a factor of 10 for a 50 % increase in thrust perturbations when adopting torque control. This also highlights the requirement to consider control strategy when analysing the transient nature of results arising from model-scale flume testing.

4.2. The effect of TI on the variability of measured quantities

Figs. 10 and 11 show the levels of variability in measured quantities, as indicated by the standard deviation, against the TI measured for each case. Fig. 10 shows the variability in Power, Torque and Thrust measured. Whereas, Fig. 11 shows the variability in rotational velocity and out-of-plane blade root bending moment. Both figures show both the measured results for speed and torque control. Within both figures both the size and colour of the plot markers are indicative of the rotational velocity for the given point. Larger and darker markers illustrate greater rotational velocities.

Whilst inspection of the above dimensional figures showed that when considering grid or wake cases in isolation the variability in rotor quantities was proportional to TI, Figs. 10 and 11 show that when considering all cases collectively, this notion cannot be generalised. Partly, this is due to the definition of TI, as outlined in Equation (2), whereby normalising the fluctuating component of a fluid velocity time series by the mean flow clearly scales the TI in proportion to the mean flow. This can be observed in Figs. 10 and 11, where, in general, Case 4 exhibits a smaller spread in measured rotor quantities that Case 2, despite a higher TI value being observed for the former case.

Further to this, the Figures illustrate that TI alone may not be a consistent indicator of the expected variability in measured quantities, not only due to the definition of the quantity, but due to it not adequately accounting for the structure of the on-coming flow. That is TI as a measurement does not adequately indicate the presence of a wake induced shear layer in the flow across the swept area of the turbine, as is the operating scenario for Case 5. Throughout Figs. 10 and 11, the variation in rotor quantities measured under Case 5 are comparable or higher than the variations measured under Case 2, despite the respective TI values measured of 9.78 % and 11.70 %. This can be clearly seen in Fig. 11B where the standard deviation in M_{YB2} for majority of operating points was equal or higher for Case 5 in comparison to Case 2. Such findings are in line with the findings discussed in Refs. [4,11] where load fluctuations of up to 40% of the time average were observed and where the requirements to understand flow structure to adequately predict loading responses were noted.

Figs. 10 and 11 highlight the differing effects of utilising speed or

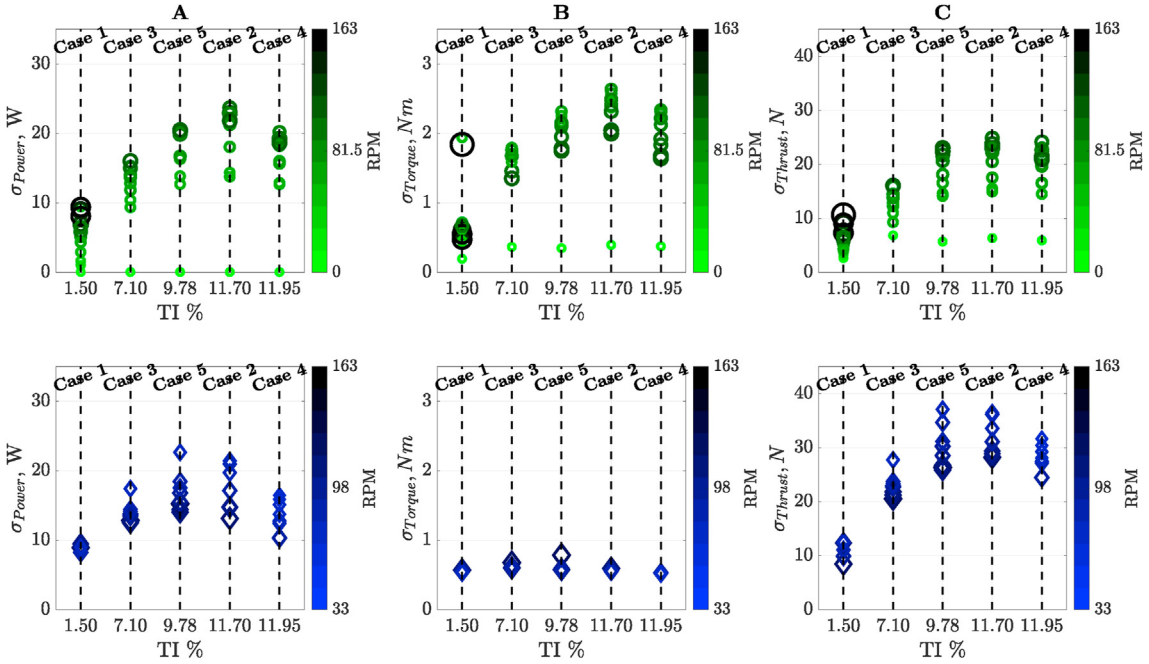

Fig. 10. Standard Deviation in measured operating parameters, utilising speed (Upper Charts) and torque control (Lower Charts), against TI. (**A**)σ_{Power} vs *TI*. (**B**)σ_{Torque} vs *TI*. (**C**)σ_{Thrust} vs *TI*. Darker larger markers indicate greater rotational velocities.

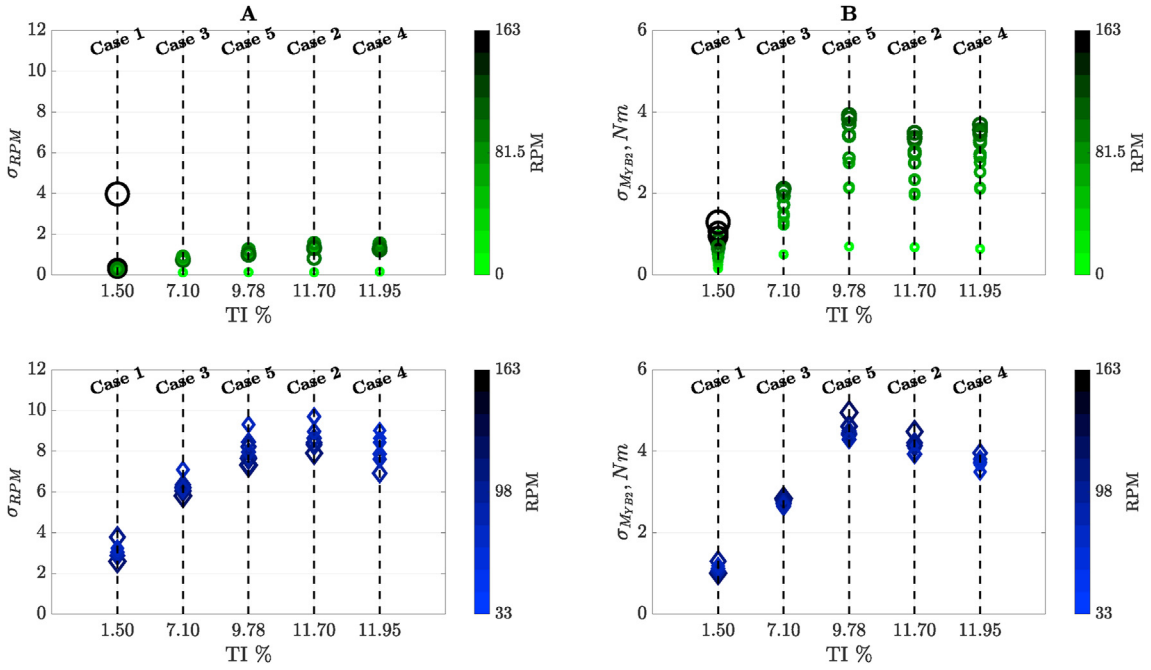

Fig. 11. Standard Deviation in measured operating parameter, utilising speed (Upper Charts) and torque control (Lower Charts), against TI. (**A**)σ_{RPM} vs *TI*. (**B**)$\sigma_{M_{YB2}}$ vs *TI*. Darker larger markers indicate greater rotational velocities.

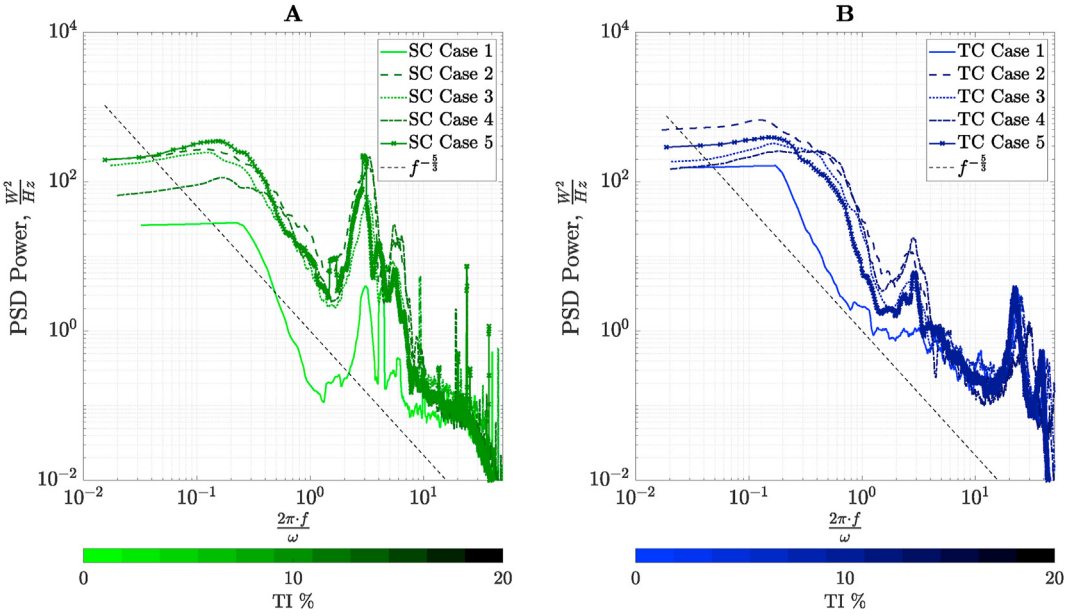

Fig. 12. Power Spectral Densities of the rotor power measured. **A** show the PSDs when Speed Control is utilised whereas the **B** show the PSDs when torque control was utilised.

torque control on the variability of the differing operational parameter measured. Clearly discernible is the amplification of the variability in thrust loading and M_{YB2} fluctuations when utilising torque control. The larger variations in rotational velocity under torque control as opposed to speed control can also be clearly observed. Conversely and arising from the definition of the differing control strategies, a larger variation in rotor torque can be observed for Cases 2 to 5 when utilising speed control - this is compared to a relatively consistent variation of approximately 0.5 Nm, when utilising torque control, over all 5 Cases. Again, similar levels of power fluctuations were observed for each control type.

4.3. Power spectral density of measured quantities

The power spectral density (PSD) of the measured, power, torque and rotational velocity a are presented in Figs. 12–14, respectively. The PSDs are calculated via the Fourier transform of the auto-correlation function for each of the measured quantities as detailed

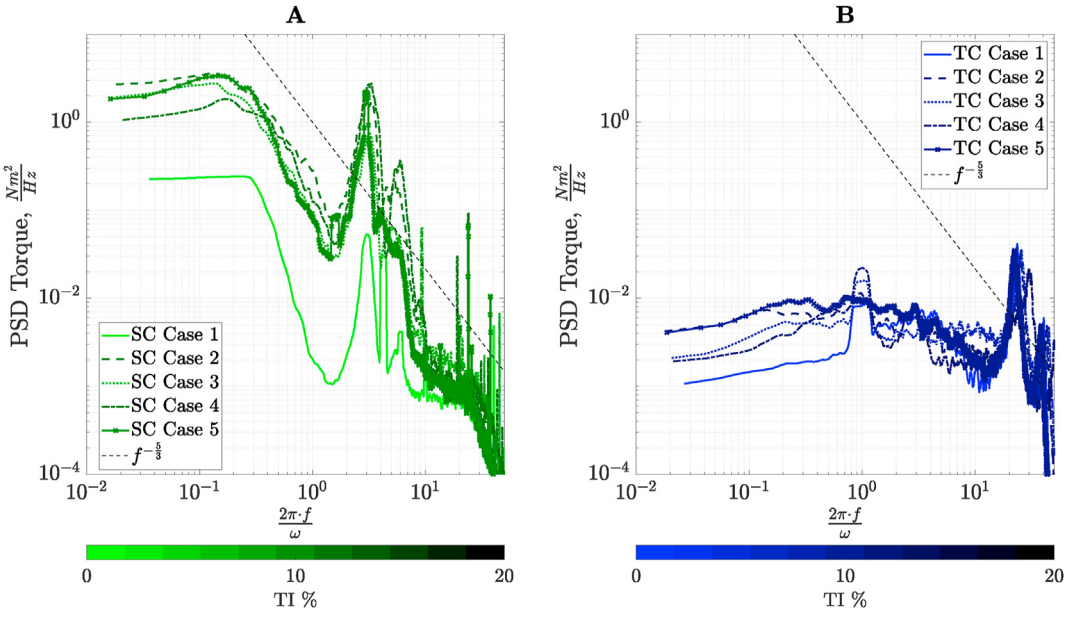

Fig. 13. Power Spectral Densities of the rotor torque measured. **A** show the PSDs when Speed Control is utilised whereas the **B** show the PSDs when torque control was utilised.

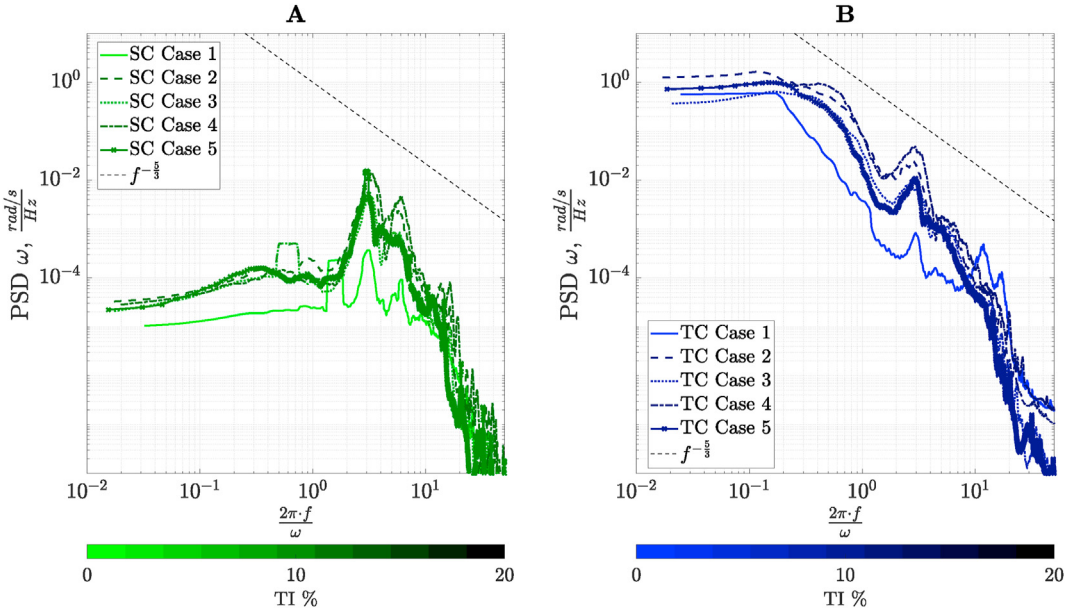

Fig. 14. Power Spectral Densities of the rotor velocity measured. **A** show the PSDs when Speed Control is utilised whereas the **B** show the PSDs when torque control was utilised.

with regard to fluid velocity measurements in Section 3.3. The figures show the PSDs of the measured quantities for each of the cases tested at a λ setting of approximately 4. The frequency axis has been scaled by the rotational velocity of the turbine to highlight any harmonics associated with the rotational velocity of the turbine.

Fig. 12 shows the PSD calculated using the rotor power measured at the lab-scale HATT for each case. The PSDs, as expected, show higher energy at lower frequencies through to lower energy at higher frequencies - the structure of the PSDs are reminiscent of the fluid velocity PSDs plotted in Fig. 5 as highlighted by the dashed $f^{-\frac{5}{3}}$ trace. The effect of differing levels of turbulence can be observed in Fig. 12A when utilising speed control. Higher TI cases generally result in higher spectral energy across all frequencies between $0.02 < \frac{2\pi f}{\omega} < 40$. A similar result can be seen when torque control is utilised, as shown in Fig. 12B, however torque control yielded higher energy a lower frequencies than the speed control counterparts. Under speed control, peaks at 3 and 6 times the rotational frequency of the turbine are clearly apparent. The amplitude of the 3rd harmonic of the rotational frequency was found to be proportional to the TI measured in all cases excluding case 5. This would suggest that the presence of a wake induced shear layer in the flow, with the turbine rotor spanning both higher and lower velocity regions, as in Case 5, leads to an amplification in the 3rd harmonic amplitude relative to the more homogeneous cases. Interestingly, this amplitudes observed in the 3rd rotational

harmonic when utilising speed control was drastically reduced when utilising torque control. This allows the increase in the observed 3rd harmonic amplitude with TI under the torque control strategy to be generalised to all cases. Higher frequency spikes observed in the speed control case exhibit the spectral shape associated with amplitude modulation and are likely to have arisen from the interaction of the control strategy and the 10 pole pairs in the PMSM. The effect of the poll pairs can also be observed in the torque control test cases, manifesting as a amplitude spike at 20 times the rotational frequency of the turbine.

Fig. 13 shows the PSD calculated using the rotor torque measured at the lab-scale HATT for each of the cases tested. Despite being an order of magnitude smaller, the structure of the rotor torque PSDs observed under speed control, Fig. 13A, are very similar to the power PSDs observed for speed control in Fig. 12A. However, the PSDs observed under torque control, Fig. 13B, vary significantly from the corresponding power PSDs presented above. A similar structure was observed in the rotor torque PSDs for all cases under torque control and were characterised as being relatively constant up to $\frac{2\pi f}{\omega} \approx 40$, other than the presence of significant amplitudes at 1 and 20 times the rotational frequency of the turbine. The low frequency content was found to be up to two orders of magnitude smaller than observed in the speed control PSDs for like cases. The amplitude observed at the first rotational harmonic of the turbine was neither consistent nor showed any particular trend across the cases tested. Again, the dominant amplitude at 20 times the rotational frequency of the HATT can be attributed to the small oscillation in torque applied via the PMSM when each pole on the rotor field passes a stator slot, known as cogging torque. Interestingly, no significant shadowing or $3 \cdot \omega$ amplitudes were observed in the torque PSDs related to torque control.

Fig. 14 shows an instance of the PSD calculated using the rotational velocity measured for each of the cases tested. Fig. 14A, which presents the results for each case under speed control, shows relatively minimal fluctuations across all frequency ranges other than prominent amplitudes at $3 \cdot \omega$ and $6 \cdot \omega$. The amplitude at $3 \cdot \omega$ is proportional to the TI for each case, excluding Case 5 where the amplitude is exaggerated due the asymmetrical shear flow impacting on the turbine. Fig. 14B shows that the structure of the fluctuations in rotational velocity observed for each case under torque control are similar in nature to the fluid spectra observed previously - highlighted by the dashed $f^{-\frac{5}{3}}$ trace. However, in comparison to the power PSDs plotted in Fig. 12, greater deviation from the dashed $f^{-\frac{5}{3}}$ trace can be observed at lower frequencies, at the 3rd harmonic of the rotational frequency of the turbine and at mid to higher frequencies ($\frac{2\pi f}{\omega} > 6$). The effect of these deviations is to produce spectra which are essentially steeper in nature than the dashed $f^{-\frac{5}{3}}$ trace developed via Kolmogorov's theory.

The relationship between the PSDs plotted in Figs. 13 and 14 highlights the reciprocal nature of the turbine operation under the speed and torque control regimes. Specifically, under speed control comparably high oscillatory energy in torque can be observed for low to mid frequencies ($\frac{2\pi f}{\omega} < 10$), whereas minimal fluctuations are observed for the same frequency range when considering the rotational velocity PSDs. The converse is true for the torque control case. The structure of these differing PSDs gives an insight into why the power PSDs have their respective structures under the differing control types. Particularly clear is the source of the significant amplitudes observed at $3 \cdot \omega$ and $6 \cdot \omega$ in the power PSDs when utilising speed control rather than torque control. The prominence in the $3 \cdot \omega$ and $6 \cdot \omega$ amplitudes arises as these amplitudes are significant in both the torque and rotational velocity spectra. The relative smoothing effect the torque control strategy has on the amplitudes at $3 \cdot \omega$ and $6 \cdot \omega$ in the power PSD arises from the smaller oscillations observed at these frequencies within the corresponding torque and rotational velocity spectra.

4.4. Spectral coherence of measured quantities

The spectral coherence between two signals is defined as the magnitude squared cross-spectral density of the two signals normalised by the product of the power spectral densities of each of the signals. The definition of the spectral coherence is defined in Equations (11) and (12), where $\rho_{xy}(t)$ is the cross-correlation function for the two variables.

$$C_{xy}(f) = \frac{|G_{xy}(f)|}{G_{xx}(f) G_{yy}(f)} \tag{11}$$

$$G_{xy}(f) = \int_{-\infty}^{\infty} \rho_{xy}(t) \cdot e^{-i\omega t} \cdot dt \tag{12}$$

Spectral coherence can be used to understand dependencies between specific quantities as they arise at differing frequencies. In linear systems, coherence can be used to define causality between differing input and output quantities, specifically for a single input to output system the coherence will be equal to unity for all frequencies. The coherence of rotor power and load quantities with the in-situ fluid velocity measurements and the rotational velocity of the turbine (inputs) has been included to help understand the interaction of control type with the complex flow fields observed throughout the five cases tested. The analysis of the coherence spectra calculated was undertaken with care as from fluid inflow to PMSM the lab-scale HATT does not constitute a linear system, as such the analysis was included to aid understanding but no formal conclusions of causality maybe drawn.

Fig. 15 shows the coherence between the rotor power and fluid velocity measured upstream of the turbine in green and the coherence between the rotor power and rotational velocity of the turbine in blue with the left chart (Fig. 15A) relating to speed control and the right chart (Fig. 15B) displaying the coherence under torque control.

Inspection of Fig. 15 shows generally poor coherence between the power produced by the turbine rotor and the fluid velocity measured 1 m upstream of the HATT. This was true for both speed and torque control for all five cases. Whilst this is clearly not true of mean power and mean fluid velocity, this lack of coherence may show that a point measurement upstream of the turbine is not suitable as an indicator of short term power fluctuations given the stochastic nature of the flow field however a comprehensive test campaign would be required to confirm this. It may also indicate a significant change in turbulent structures from LDV measurement position to the turbine rotor - again leading to upstream point measurements being ineffective for prediction of short term power oscillations. This finding is supported given the mean velocity, TI and $\mathscr{L}_x$ gradients observed in both the grid and turbine wake cases, see Figs. 3 and 4. Lastly, this finding is relatively surprising under speed control operation where the rotational velocity is

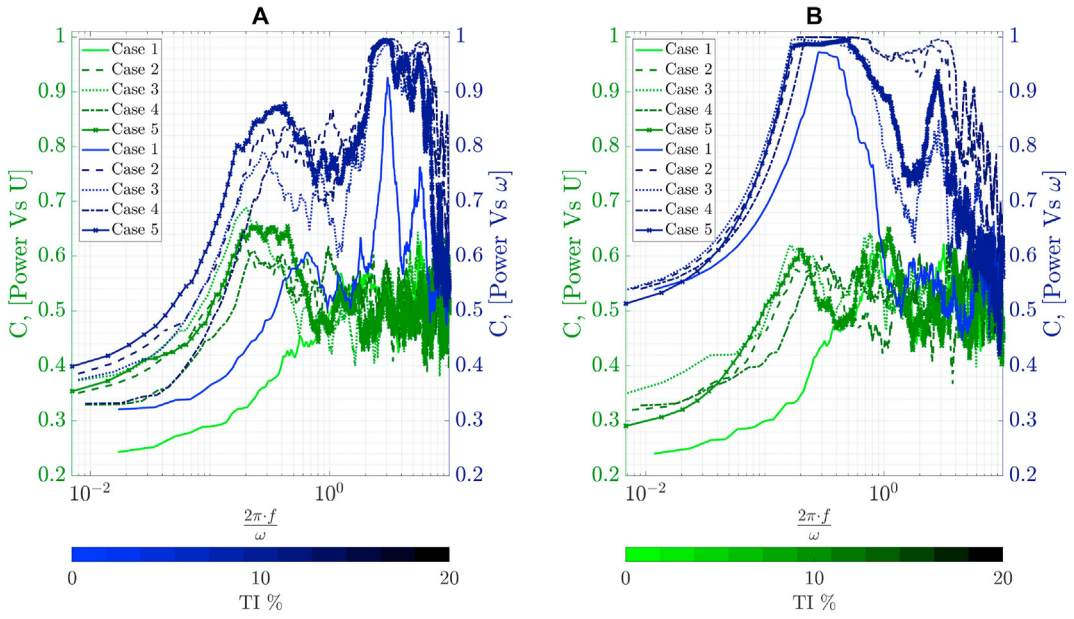

Fig. 15. Plots showing the spectral cohesion between Power and mean fluid velocity (green trace), as well as the spectral cohesion between Power and rotational velocity (blue trace). (**A**) Speed Control. (**B**) Torque Control. (For interpretation of the references to colour in this figure legend, the reader is referred to the Web version of this article.)

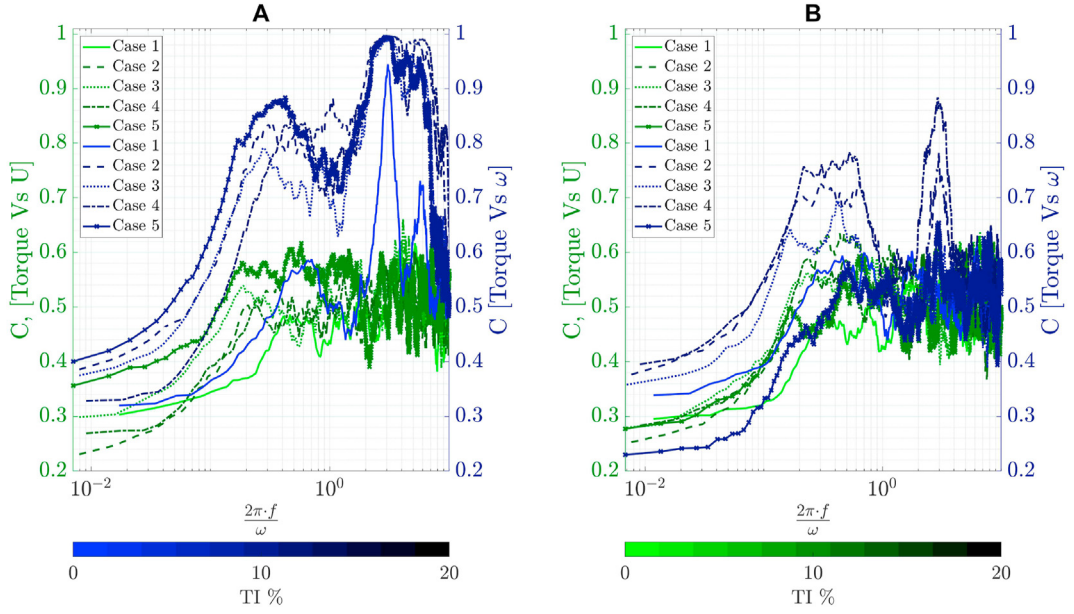

Fig. 16. Plots showing the spectral cohesion between Torque and mean fluid velocity (green trace), as well as the spectral cohesion between Torque and rotational velocity (blue trace). (**A**) Speed Control. (**B**) Torque Control. (For interpretation of the references to colour in this figure legend, the reader is referred to the Web version of this article.)

approximately constant. As such, it would be expected that most power fluctuations were driven purely by fluid velocity fluctuations - both in terms of power flux variations within the fluid and variations in angle of attack.

Under speed control a strong coherence was found between the rotor power and rotational velocity of the turbine at the 3• ω and 6• ω harmonics. This was coupled with a relatively strong coherence between the two aforementioned quantities at lower frequencies. The breath and degree of the coherence of lower frequencies appears to be proportional to the TI recorded for each case with the coherence at the 3•ω and 6•ω frequencies remaining relatively consistent across Cases 2 to 5, suggesting a weaker effect of TI on the coherence at 3•ω and 6•ω. The strong coherence in terms of rotor power and rotational velocity of the turbine at the 3•ω and 6•ω harmonics observed under speed control suggests a deeper dependence on the control of the model HATT. Upon blade passing events it is likely that a small oscillation in rotational velocity occurs as the PI controller compensates for the change in the system operation. These oscillations yield a 2-degree dependency of the rotor power on the rotational velocity of the turbine. Initially, there

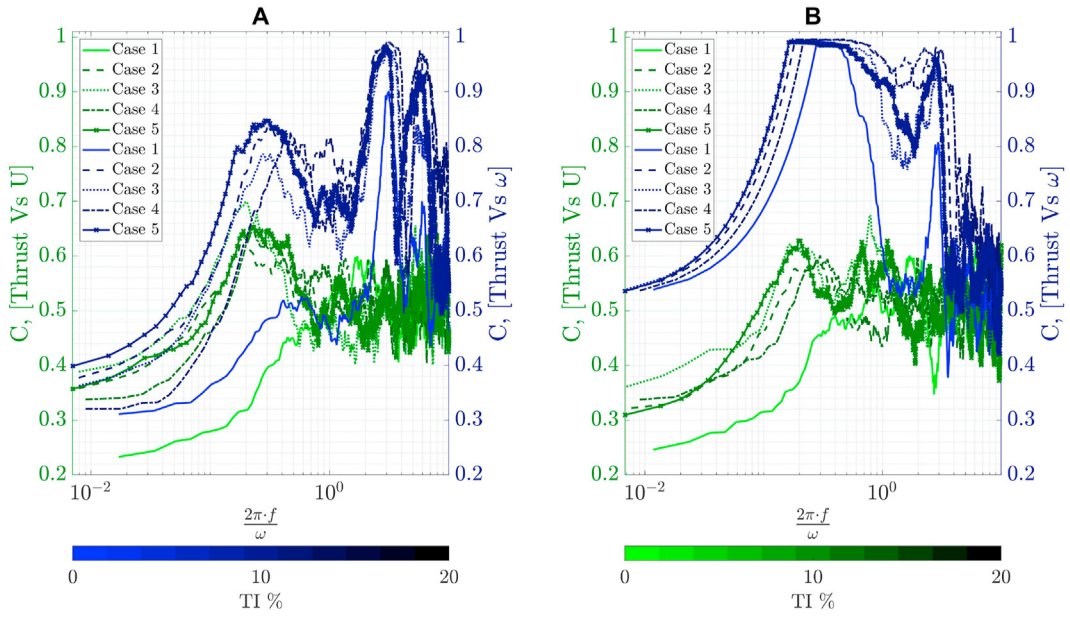

Fig. 17. Plots showing the spectral cohesion between Thrust and mean fluid velocity (green trace), as well as the spectral cohesion between Thrust and rotational velocity (blue trace). (**A**) Speed Control. (**B**) Torque Control. (For interpretation of the references to colour in this figure legend, the reader is referred to the Web version of this article.)

is a strong direct coupling due to the definition of the power generated via the rotor and secondly a weaker but substantial coupling exists due to the relatively large fluctuations in angle of attack created by rotational velocity fluctuations. This notion is supported in Fig. 16, where under speed control there is a strong coherence between the torque developed at the turbine rotor and the rotational velocity of the turbine, clearly resulting from the aforementioned oscillation in angle of attack.

Under torque control strong coherence between the rotor power and rotational velocity was found at lower frequencies, this coherence was significantly greater than under speed control. This strong cohesion between rotor power and rotational velocity highlights the direct dependency of rotor power on rotational velocity. The lack of cohesion observed in Fig. 16 between the rotor torque and rotational velocity highlights the tendency of the rotor to accelerate or decelerate to maintain a fixed rotor torque opposing the braking torque applied by the PMSM. The rotor torque is maintained by changes in angle of attack which vary lift out of phase with the fluid velocity impacting the rotor - this is clear when considering the shape of the non-dimensional torque curves presented in Figs. 7 and 8 for the torque control cases. Again, the degree and breadth of the coherence appears to be related to the TI for

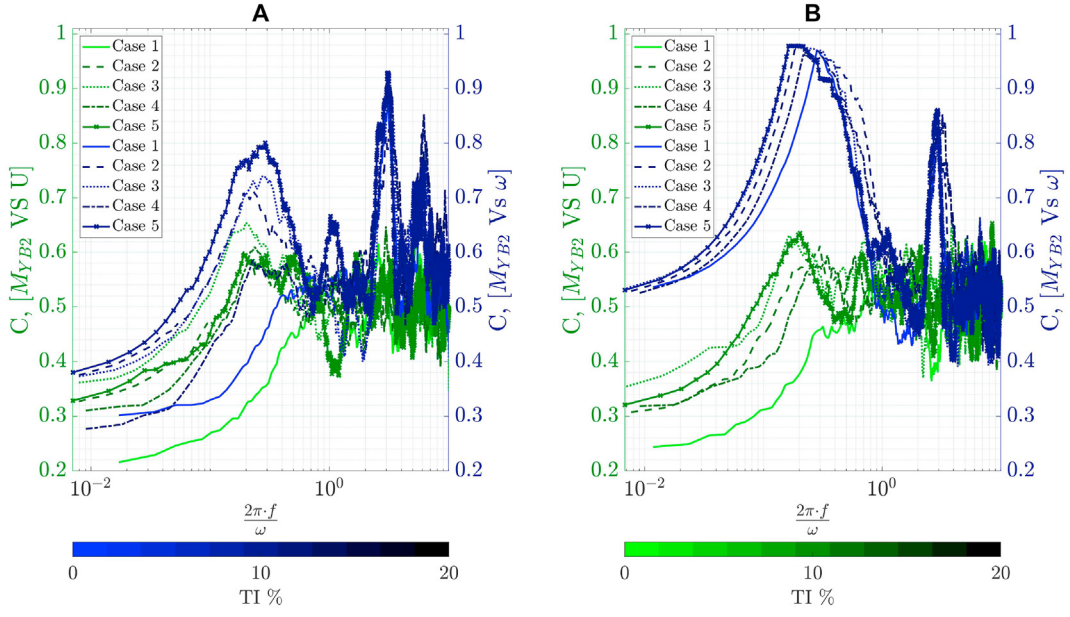

Fig. 18. Plots showing the spectral cohesion between M_{YB2} and mean fluid velocity (green trace), as well as the spectral cohesion between M_{YB2} and rotational velocity (blue trace). (**A**) Speed Control. (**B**) Torque Control. (For interpretation of the references to colour in this figure legend, the reader is referred to the Web version of this article.)

each case, other than Case 5. Clearly, oscillations in the rotational velocity are driven by variations, both spatially and temporally, in the flow impacting the turbine. However, as highlighted above, a point measurement 1 m upstream of the turbine is not an adequate indicator of the complex flow impacting the turbine rotor. The relationship between the measured TI and the low frequency cohesion discussed supports the intuitive findings described, whereby the anomaly observed for Case 5 is likely to have arisen from the HATT operation within the wake induced shear region as shown in Fig. 4**A**.

Fig. 17 shows the coherence between the rotor thrust and fluid velocity measured upstream of the turbine and the coherence between the rotor thrust and rotational velocity of the turbine, the labelling convention is the same as described above for Fig. 15. The coherence spectra shown within Fig. 17 shows limited cohesion between rotor thrust and the fluid velocity measured 1 m upstream of the device; the largest coherence values were found between $0.2 < \frac{2\pi f}{\omega} < 0.8$ which ranged from 0.6 to 0.65, these find were consistent in amplitude with those observed in Ref. [11,12] albeit across differing frequency ranges as dictated by the shedding frequency or turbulence characteristics associated with the setup. In terms of the coherence between measured rotor thrust and rotational velocity a similar coherence structure can be observed as seen in the coherence between the rotor power and rotational velocity of the turbine. Again, under speed control the coherence between the two quantities is strongest at the harmonics of the rotational speed of the turbine; whereas under torque control the strongest cohesion was generally observed at low frequencies. The degree and frequency range of the strong cohesion at lower frequencies under torque control is generally proportional to the TI measured. Intuitively, this finding helps describe the larger fluctuation in rotor thrust loading under torque control rather than under speed control whereby the oscillations in rotor thrust loading are likely to be predominately linked to changes in angle of attack and relative fluid velocity which are in turn driven by changes in the rotational speed of the turbine.

Lastly, Fig. 18 shows the cohesion between both the fluid velocity and rotor velocity and the out-of-plane blade RBM measured for blade 2. Again the same labelling convention as discussed with reference to Fig. 15 applies. As expected a similar overall structure of the cohesion plots can be observed relative to the cohesion plots presented for the rotor thrust loading in 17. However, there are some clear discrepancies, in terms of speed control the coherence at $3 \cdot \omega$ shows greater cohesion than at $6 \cdot \omega$ which is not generally the case when considering the thrust loading under speed control. Under torque control both thrust and RBM cohesion plots exhibit strong cohesion at low frequencies. However, the range of frequencies over which the strong cohesion was observed is reduced in the RBM plots creating a more peaked cohesion at lower frequencies. The more peaked cohesion at lower frequencies exposes a consistent and relatively strong cohesion at $3 \cdot \omega$.

5. Conclusions

The paper considered the effects of differing operating scenarios on the power output and loading characteristics observed for a lab scale HATT. The campaign presented showed that it may well be possible to exploit the accelerated region around an upstream turbine to capture marginally higher power (6% increase) from downstream turbines. It was also found that this may still be true if the wake of the upstream turbine impacts a portion of the downstream rotor. It was observed that operating a HATT directly in the wake of an upstream turbine yields a 52 % reduction in mean power output relative to operating partially with the upstream device's wake. Interestingly, similar levels of oscillation for were observed in both cases.

The results presented would suggest that TI may be a good indicator of the size of rotor load fluctuations when the stream wise velocity and TI are homogeneous. However, under the effect of a shear layer as introduced by the wake of the upstream turbine, Case 5, TI can lead to underestimation of load fluctuations.

Analysis of data captured under set-point speed and torque control strategies showed that under torque control a significant reduction, up to 10 times, in rotor torque oscillations could be observed for a 50% increase in thrust oscillations. Furthermore, the control strategy utilised had little effect on the mean values of power, thrust and torque developed by the turbine. The largest increase in thrust oscillations observed when comparing torque control to speed control was observed in the Case 5, which was likely to have been caused by the presence of the shear layer.

Analysis of the power spectral density of the measured quantities showed the relative adherence of the rotor quantities to the turbulence spectra observed. Notable exceptions to this finding were the PSD of the rotor torque developed under torque control and the PSD of the rotor velocity under speed control. Here the PSD was of the rotor torque was flattened highlighting that at this inertial scale the acceleration of the turbine tended to reduce torque fluctuations. Conversely under speed control the PSD of the rotational velocity deviated from the fluid spectra observed as the control system maintained a fixed rotational velocity.

Lastly, analysis of the spectral cohesion between measured quantities was used to help understand the dependency between variables. Whilst, in general the shape of the measured fluid velocity PSDs followed a similar trend to the rotor quantities measured, with the exceptions noted above, the LDV measurement 1 m upstream of the turbine showed mediocre spectral cohesion with the measured rotor quantities. This would suggest that single point upstream measurements maybe a poor predictor of short term load fluctuations. Generally higher spectra cohesion of the rotor loads where found relative to the rotor velocity - this would suggest that changes in rotational velocity are dominant in changing instantaneous angle of attack particularly in the torque control case. Provided the device is operating above the stall region, changes in angle of attack caused by changes in rotational velocity could be significant in driving changes in the lift developed by the each blade. These lift oscillations will be the dominant factor in rotor loads at the specified operating conditions. Such an assertion is based on the reasoning presented in Ref. [6] and indeed assumes large λ-values, in this regard further study is needed to refine this conclusion.

Declaration of competing interest

The authors declare that they have no known competing financial interests or personal relationships that could have appeared to influence the work reported in this paper.

Acknowledgements

Funding: This work was supported by the Engineering and Physical Sciences Research Council [DyLoTTA – EP/N020782/1]; Engineering and Physical Sciences Research Council [Cardiff University Impact Acceleration Account-EP/R51150X/1]. The data underpinning this article can be accessed at: https://doi.org/10.17035/d.2020.0124287467.

Appendix A. Turbulence Grid Details

The turbulence generating grid utilised was constructed to the dimensions presented in Fig. A.19 as initially presented by Ref. [4].

References

[1] M. Allmark, R. Ellis, C. Lloyd, S. Ordonez-Sanchez, K. Johannesen, C. Byrne, C. Johnstone, T. O'Doherty, A. Mason-Jones, The development, design and characterisation of a scale model Horizontal Axis Tidal Turbine for dynamic load quantification, Renew. Energy 156 (2020) 913–930, https://doi.org/10.1016/j.renene.2020.04.060.

[2] M.J. Allmark, Condition Monitoring and Fault Diagnosis of Tidal Stream Turbines Subjected to Rotor Imbalance Faults (Ph.D. thesis.), 2016.

[3] T. Blackmore, B. Gaurier, L.E. Myers, G. Germain, A.S. Bahaj, The effect of freestream turbulence on tidal turbines, in: Proceedings of the 11th European Wave and Tidal Energy Conference 6-11th Sept 2015 vol. 53, 2015, pp. 1–10, https://doi.org/10.1017/CBO9781107415324.004. Nantes, France.

[4] T. Blackmore, L.E. Myers, A.S. Bahaj, Effects of turbulence on tidal turbines: implications to performance, blade loads, and condition monitoring, International Journal of Marine Energy 14 (2016) 1–26, https://doi.org/10.1016/j.ijome.2016.04.017.

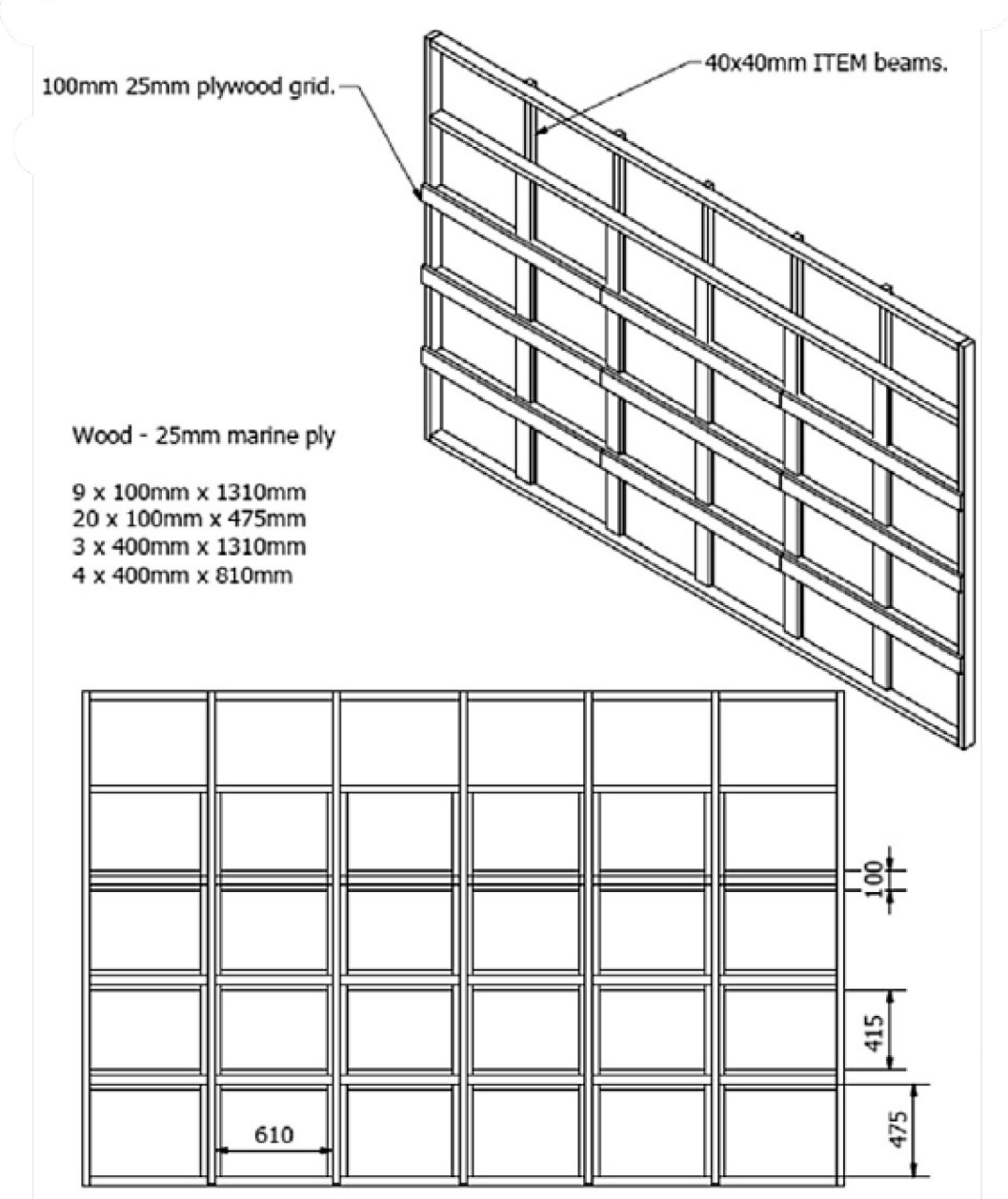

Fig. A.19. Dimensions of the turbulence generating grid originally developed by Ref. [4]

[5] P.P. Bradshaw, An Introduction to Turbulence and its Measurement, Pergamon Press, 1971.
[6] T. Burton, N. Jenkins, D. Sharpe, E. Bossanyi, Design loads for horizontal Axis wind turbines, in: Wind Energy Handbook, John Wiley & Sons, Ltd, 2011, pp. 193–323, https://doi.org/10.1002/9781119992714.ch5.
[7] G. Deskos, G.S. Payne, B. Gaurier, M. Graham, On the spectral behaviour of the turbulence-driven power fluctuations of horizontal-axis turbines, J. Fluid Mech. (2020), https://doi.org/10.1017/jfm.2020.681.
[8] T. Ebdon, The Impact of Turbulence and Turbine Operating Condition on the Wakes of Tidal Turbines (Ph.D. thesis), 2019.
[9] D. of Energy, C. Change, UK Renewable Energy Roadmap Update 2013, 2013, p. 76.
[10] European Parliament, Directive (EU) 2018/2001 of the European Parliament and of the Council of 11 December 2018 on the Promotion of the Use of Energy from Renewable Sources, European Parliament and Council of 11 December 2018, London, 2018. Technical Report.
[11] B. Gaurier, C. Carlier, G. Germain, G. Pinon, E. Rivoalen, Three tidal turbines in interaction: an experimental study of turbulence intensity effects on wakes and turbine performance, Renew. Energy 148 (2020a) 1150–1164, https://doi.org/10.1016/j.renene.2019.10.006.
[12] B. Gaurier, M. Ikhennicheu, G. Germain, P. Druault, Experimental study of bathymetry generated turbulence on tidal turbine behaviour, Renew. Energy 156 (2020b) 1158–1170, https://doi.org/10.1016/j.renene.2020.04.102.
[13] M. Harrold, P. Ouro, T. O'Doherty, Performance assessment of a tidal turbine using two flow references, Renew. Energy 153 (2020) 624–633, https://doi.org/10.1016/j.renene.2019.12.052.
[14] C.M. Johnstone, D. Pratt, J.A. Clarke, A.D. Grant, A techno-economic analysis of tidal energy technology, Renew. Energy 49 (2013) 101–106, https://doi.org/10.1016/j.renene.2012.01.054.
[15] A. Kolmogorov, The local structure of turbulence in incompressible viscous fluid for very large Reynolds numbers, Proceedings of the USSR Academy of Sciences 30 (1941) 299–303.
[16] C. Lloyd, The Performance of a Tidal Stream Turbine under Wave and Current Interaction, Ph.D. thesis, 2020.
[17] F. Maganga, G. Germain, J. King, G. Pinon, E. Rivoalen, Experimental characterisation of flow effects on marine current turbine behaviour and on its wake properties, IET Renew. Power Gener. 4 (2010) 498–509, https://doi.org/10.1049/iet-rpg.2009.0205.
[18] R. Martinez, S. Ordonez-Sanchez, M. Allmark, C. Lloyd, T. O'Doherty, G. Germain, B. Gaurier, C. Johnstone, Analysis of the effects of control strategies and wave climates on the loading and performance of a laboratory scale horizontal axis tidal turbine, Ocean. Eng. 212 (2020) 107713, https://doi.org/10.1016/j.oceaneng.2020.107713.
[19] A. Mason-Jones, D.M. O'Doherty, C.E. Morris, T. O'Doherty, Influence of a velocity profile & support structure on tidal stream turbine performance, Renew. Energy 52 (2013) 23–30, https://doi.org/10.1016/j.renene.2012.10.022.
[20] P. Mycek, B. Gaurier, G. Germain, G. Pinon, E. Rivoalen, Experimental study of the turbulence intensity effects on marine current turbines behaviour. Part I: one single turbine, Renew. Energy 66 (2014a) 729–746, https://doi.org/10.1016/j.renene.2013.12.036.
[21] P. Mycek, B. Gaurier, G. Germain, G. Pinon, E. Rivoalen, Experimental study of the turbulence intensity effects on marine current turbines behaviour. Part II: two interacting turbines, Renew. Energy 68 (2014b) 876–892, https://doi.org/10.1016/J.RENENE.2013.12.048. URL: https://www.sciencedirect.com/science/article/pii/S0960148114000196.
[22] L. Myers, A. Bahaj, Near wake properties of horizontal axis marine current turbines, in: 8th European Wave and Tidal Energy Conference, 2009, pp. 558–565.
[23] L.E. Myers, A.S. Bahaj, Experimental analysis of the flow field around horizontal axis tidal turbines by use of scale mesh disk rotor simulators, Ocean. Eng. 37 (2010) 218–227, https://doi.org/10.1016/j.oceaneng.2009.11.004.
[24] S. Ordonez-Sanchez, M. Allmark, K. Porter, R. Ellis, C. Lloyd, I. Santic, T. O'Doherty, C. Johnstone, S. Ordonez-Sanchez, M. Allmark, K. Porter, R. Ellis, C. Lloyd, I. Santic, T. O'Doherty, C. Johnstone, Analysis of a horizontal-Axis tidal turbine performance in the presence of regular and irregular waves using two control strategies, Energies 12 (2019) 367, https://doi.org/10.3390/en12030367. URL: http://www.mdpi.com/1996-1073/12/3/367.
[25] S. Ordonez-Sanchez, K. Porter, C. Frost, M. Allmark, C. Johnstone, Effects of wave-current interactions on the performance of tidal stream turbines, Proceedings of the 3rd Asian Wave & Tidal Energy Conference 394 (2016), https://doi.org/10.3850/978-981-11-0782-5.
[26] S.E. Ordonez-Sanchez, K. Porter, R. Ellis, C. Frost, M. Allmark, T. Nevalainen, T. O'Doherty, C. Johnstone, Numerical Modelling Techniques to Predict Rotor Imbalance Problems in Tidal Stream Turbines, 2017.
[27] K. Porter, S. Ordonez-sanchez, M. Allmark, R. Ellis, C. Lloyd, O. Doherty, C. Johnstone, Laboratory study of tidal turbine performance in irregular waves, in: Proceedings of the 4th Asian Wave and Tidal Energy Conference, 2018.
[28] G.I. Taylor, Statistical theory of turbulence, Proc. Roy. Soc. Lond. Math. Phys. Sci. 151 (1935) 421–444.
[29] H.H. Tennekes, J.L.J.L. Lumley, A First Course in Turbulence, 1972.